

# Coexistence of Self-Organized Criticality and Intermittent Turbulence in the Solar Corona

Vadim M. Uritsky,<sup>1,\*</sup> Maya Paczuski,<sup>1</sup> Joseph M. Davila,<sup>2</sup> and Shaela I. Jones<sup>3</sup>

<sup>1</sup>*Complexity Science Group, Department of Physics and Astronomy,  
University of Calgary, Calgary, Alberta, Canada T2N 1N4*

<sup>2</sup>*NASA Goddard Space Flight Center, Greenbelt, MD 20771, USA*

<sup>3</sup>*University of Maryland, College Park, MD 20742, USA*

(Dated: September 24, 2018)

An extended data set of extreme ultraviolet images of the solar corona provided by the SOHO spacecraft are analyzed using statistical methods common to studies of self-organized criticality (SOC) and intermittent turbulence (IT). The data exhibits simultaneous hallmarks of both regimes, namely power law avalanche statistics as well as multiscaling of structure functions for spatial activity. This implies that both SOC and IT may be manifestations of a single complex dynamical process entangling avalanches of magnetic energy dissipation with turbulent particle flows.

PACS numbers: 05.65+b, 52.35.Ra, 96.60.qe

SOC and IT represent two paths to dynamical complexity in driven, extended nonlinear systems. In classical fluid turbulence, scaling is often associated with a hierarchical structure of eddies extending over the inertial range [1], while in SOC, avalanches of localized instabilities organize the system toward a steady state exhibiting long-range correlations up to the system size [2]. Some authors have argued that SOC and IT are distinct, unrelated phenomena [3, 4, 5], while others have suggested a fundamental connection [6, 7, 8, 9, 10]. In fact, Bak and co-workers have speculated that turbulence in the limit of high Reynolds number (HRN) may itself be a SOC phenomenon [6, 11, 12], with dynamical transitions observed in HRN turbulence being critical avalanches of dissipation. It has also been shown [10] that, in contrast to earlier claims [3], SOC and IT cannot be distinguished by analyzing interoccurrence times between bursts: once a finite observation threshold (unavoidable in any physical measurement) is introduced, even the ordinary BTW sandpile exhibits scale free waiting time statistics [10] indicative of turbulent systems.

We propose that coexistence of SOC and IT may be a generic feature of magnetized astrophysical plasmas. One scenario for this to occur is localized instabilities [13, 14, 15] switching the plasma between frozen and unfrozen states. This process resembles stick-slip or depinning transitions of SOC models [16, 17] and is to some extent analogous to rice pile dynamics [18], where kinetic energy of grains releases stored potential energy. Signatures of SOC and IT have also been obtained in MHD simulations [19, 20, 21] mimicking footpoint motions of coronal magnetic loops. However, the explicit complementarity between SOC and IT in astrophysical observations has not been demonstrated.

In order to clarify this issue, we present direct observational evidence for coexistence of SOC and IT in the magnetized plasma of the solar corona. Using a single high resolution data set, we apply two different analysis meth-

ods – one for analyzing avalanche statistics of the emission field and the other for analyzing structure functions of the same field. The energy, area and lifetime statistics of avalanches detected in this data set obey robust scaling laws. Unlike previous studies of flare statistics, we use a spatiotemporal event detection algorithm compatible with the usual definition of avalanches in SOC. Next, we show that the same data set exhibits multiscaling and extended self-similarity (ESS) of higher order structure functions – a hallmark of IT phenomena. The observed scaling laws show only weak dependence on average solar activity and were found both at solar minimum (min) and maximum (max), indicating that coexistence of SOC and IT is a generic characteristic of coronal behavior.

Dissipation mechanisms in the corona are activated by changes in the configuration of its magnetic field. Convection of magnetic fields leads to radiative transients, plasma jets, and explosive events known as flares [22, 23, 24]. The latter are associated with spatially concentrated release of magnetic energy accompanied by localized plasma heating up to temperatures of  $10^7\text{K}$ , and can be observed by short-wavelength light emission. Flares tend to appear at irregular times and locations and exhibit broadband energy, size and lifetime statistics with no obvious characteristics scales. This behavior is often interpreted as a signature of SOC [25, 26, 27, 28, 29, 30]. Further, the configuration of magnetic flux in the corona has been shown to form a scale-free network with statistical features that can be captured with a self-organizing network model [30]. Within active regions, the magnetic field also has an intermittent spatial structure that reorganizes during large flares [31]. Our results suggest, though, that complementary coexistence of SOC and IT is a generic phenomenon not limited to these large events.

We have studied time series of full-disk digital images of the corona taken by the extreme ultraviolet imaging telescope (EIT) onboard the SOHO spacecraft [24] in the  $195\text{ \AA}$  wavelength band corresponding to the Fe

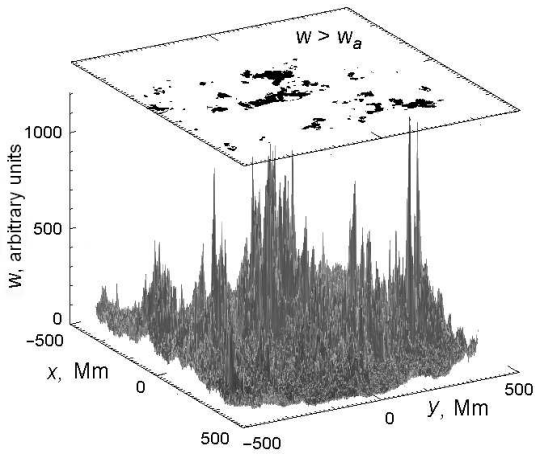


FIG. 1: Two views of the corona's complexity. Upper panel: snapshots of high activity coronal regions used to construct avalanches ( $w_a = 350$ ). Lower panel: a snapshot of the continuous brightness field at the same time instant.

XII emission at peak coronal temperatures of  $1.6 \cdot 10^6$  K. The data included two observation periods: 06/29/2001 - 07/28/2001 (3240 images, solar max, average sunspot number 64.0) and 10/22/2005 - 12/02/2005 (4407 images, solar min, average sunspot number 16.3) with a typical time resolution of 13.3 min. To reduce optical distortions, we studied only central portion of the Sun disk with the linear dimensions  $1040 \times 1040$  Mm ( $256 \times 256$  pixels with 5.6 arcsec resolution). The EIT luminosity  $w(t, \mathbf{r})$  was analyzed as a function of time  $t$  and position  $\mathbf{r}$  on the image plane. The dynamics of  $w(t, \mathbf{r})$  captures the redistribution of radiative flux in consecutive EIT frames due to a variety of coronal features such as loops and holes, mass ejections, etc. For the purpose of this study, we treated  $w(t, \mathbf{r})$  as a local measure of coronal activity and did not filter the data in an attempt to distinguish between different types of coronal events. Our analysis was based on two alternative approaches allowing a study of  $w(t, \mathbf{r})$  both as an impulsive avalanching process and a continuum turbulent field – as shown in Fig. 1.

To identify avalanches, we used a spatiotemporal detection method [32, 33] that resolves concurrent events. First, avalanching regions were identified by applying an activity threshold  $w_a$  representing a background EUV flux. Contiguous spatial regions with  $w(\mathbf{r}, t) > w_a$  were treated as pieces of evolving avalanches. By checking for overlap of common pixels between each pair of consecutive EIT frames, we identified a set of 3-dimensional spatiotemporal integration domains  $\Lambda_i (i = 1, \dots, N)$  corresponding to each of  $N$  individual avalanches. These domains of contiguous activity in space and time were used to compute the lifetimes,  $T_i = \max(t \in \Lambda_i) - \min(t \in \Lambda_i)$ , the radiative emission flux,  $E_i = \int_{\Lambda_i} w(\mathbf{r}, t) d\mathbf{r} dt$ , as well the peak areas,  $A_i = \max_t (\int_{\Lambda_i(t)} d\mathbf{r})$ , or maximum number of pixels in a snapshot of each avalanche. Active regions that split after starting at a unique source were

considered parts of a single avalanche. Active regions that merged were considered as separate avalanches, with the common "tail" ascribed to the event that started earlier. Only events that lasted at least two successive time frames and were not truncated by the field of view or temporal gaps in observations longer than 40 min were selected for subsequent analysis. The robustness of the obtained statistics was verified by repeatedly running the algorithm with substantially different  $w_a$ . Due to large difference in average emission,  $\langle w \rangle$ , during solar min and max,  $w_a$  were defined relative to  $\langle w \rangle$  for each data set. Depending on  $w_a$ , between 4,830 (1,680) and 26,900 (5,350) coronal events were detected for solar max (min).

Fig. 2 shows probability distributions for avalanche lifetime, total emission flux and peak area for both solar max and min. These statistics can be approximately fitted by the power-law relations  $p(T) \sim T^{-\tau_T}$ ,  $p(E) \sim E^{-\tau_E}$  and  $p(A) \sim A^{-\tau_A}$  with the exponents being almost independent of  $w_a$ . The same exponents have also been found using a fluctuating threshold placed at 3 standard deviations above the average brightness of each image. The large-scale rollovers are due to the lack of events whose  $T$  approaches the maximum available time scale  $5.2 \cdot 10^5$ s given by the ratio between the latitudinal size of the field of view and the rotation velocity at the equator. Such events tend to cross the field of view and are therefore underrepresented in our sample.

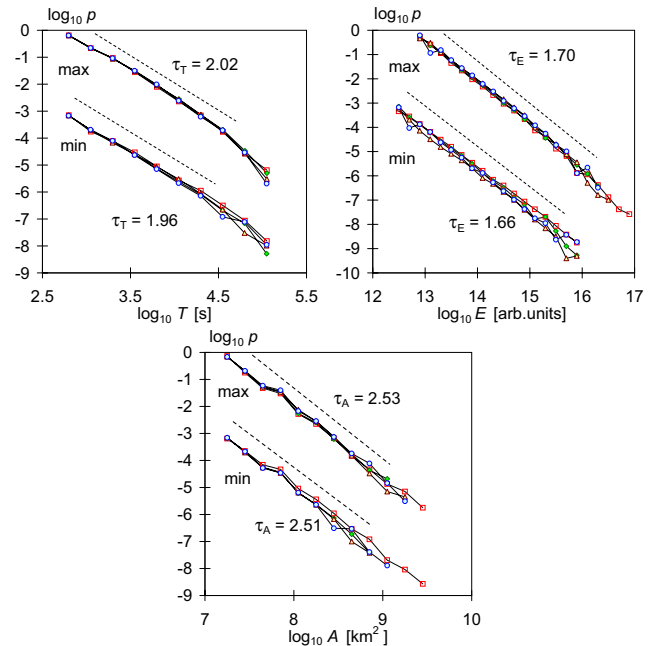


FIG. 2: Probability distributions of avalanche lifetime, emission flux and peak area for solar max and min at four different thresholds  $w_a = k \langle w \rangle$  with  $k = 0.4$  (squares),  $k=0.8$  (diamonds),  $k=1.2$  (triangles) and  $k=1.6$  (circles). The min distributions are shifted downward for comparison.

The exponents observed at solar max ( $\tau_T = 2.02 \pm 0.05$ ,  $\tau_E = 1.70 \pm 0.04$ ,  $\tau_A = 2.53 \pm 0.09$ ) and at solar min

( $\tau_T = 1.96 \pm 0.06$ ,  $\tau_E = 1.66 \pm 0.03$ ,  $\tau_A = 2.51 \pm 0.14$ ) are indistinguishable within uncertainties. This is also true for the exponents  $z$ ,  $D_E$  and  $D_A$  defined by the relations  $T \sim l^z$ ,  $E \sim l^{D_E}$  and  $A \sim l^{D_A}$ , where  $l$  is the linear avalanche scale [47]. The resulting values are  $z = 1.94 \pm 0.12$ ,  $D_E = 3.16 \pm 0.21$  and  $D_A = 1.50 \pm 0.10$  for solar max and  $z = 2.09 \pm 0.17$ ,  $D_E = 3.34 \pm 0.25$  and  $D_A = 1.52 \pm 0.11$  for solar min. All values were obtained by averaging over four activity thresholds ( $w_a = k \langle w \rangle$ , where  $k \in \{0.4, 0.8, 1.2, 1.6\}$ ) within fixed ranges of scales corresponding to the power-law portions of the relations. The reported uncertainties are the standard errors from this averaging or from the regression estimate at individual thresholds, whichever is larger. Up to these errors, the exponents satisfy the probability conservation relations  $z(\tau_T - 1) = D_E(\tau_E - 1) = D_A(\tau_A - 1)$ .

All these results support the hypothesis that the corona operates in a SOC state. It is worth emphasizing that the exponents reported here have been obtained using spatiotemporal definition of avalanches which is conceptually much closer to measuring avalanches in numerical simulations than most of the definitions used in previous works on flare statistics – except for a few case studies [23, 28] focusing on specific coronal conditions. The energy distribution exponent  $\tau_E$  is smaller than 2 indicating that the coronal heating is dominated by large events as opposed to Parker’s scenario of nanoflare heating [34]. This conclusion is in agreement with previous estimates based on spatiotemporal detection of coronal brightenings [23, 28] and their spatial detection with subsequent integration of the emission fluxes over fixed time interval [22, 26]. The exponent  $D_A$  matches the fractal dimension of nanoflares reported in [26], whereas  $\tau_T$  is consistent with previous analyses of threshold-dependent inter-occurrence times of x-ray bursts measured over the whole Sun [35], as would be expected if total emission were a sum over individual avalanches [36]. Its value as well as  $z \approx 2$  indicate that the corona may operate at a mean-field limit [37]. We also note that the avalanche exponents reported are consistent with the results of forced MHD simulation of turbulent coronal heating [19].

As our next step, we have analyzed coronal activity as a continuum turbulent field. Such analyses are normally accomplished by measuring structure functions [38] for a relevant dynamical variable  $\delta z$ . Taking  $\delta z$  proportional to differences in the scalar field  $w(\mathbf{r}, t)$  [39], we define the structure functions of order  $q$  to be

$$S_q(l) = \langle |w(\mathbf{r}, t) - w(\mathbf{r} + \delta\mathbf{r}, t)|^q \rangle_{\mathbf{r}} \quad (1)$$

Here  $\delta\mathbf{r}$  is the spatial displacement,  $l \equiv |\delta\mathbf{r}|$ , and averaging indicated by brackets is performed over all positions  $\mathbf{r}$ . Within the inertial range,  $S_q(l) \sim l^{\zeta(q)}$  with  $\zeta(q)$  defined by the turbulent regime under study. In practice, scaling directly in  $S_q(l)$  is often limited in range. This is exactly the issue we faced when analyzing the coronal images (Fig. 3). In such situations, the ESS method [40]

is often used which allows to extend the observed range of turbulent scaling making it possible to estimate relative exponents [48]. The non-trivial behavior of the moments is approximately isotropic within uncertainties (see the inset in Fig. 4) and so could not be eliminated by projecting the data onto irreducible representations of a lower symmetry group [38].

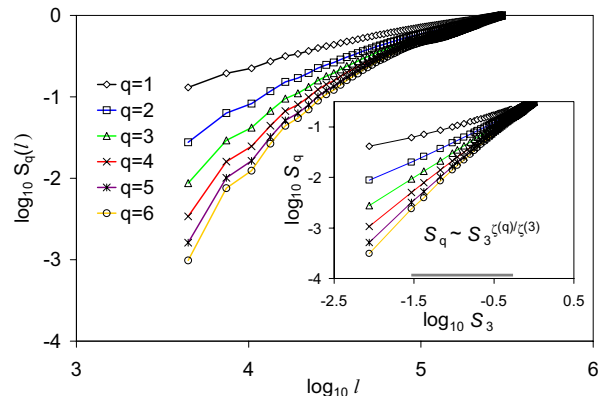


FIG. 3: Structure functions of coronal activity. Each function is normalized by its maximum value. Inset: ESS scaling of the structure functions. The horizontal bar shows the range used for estimating exponents.

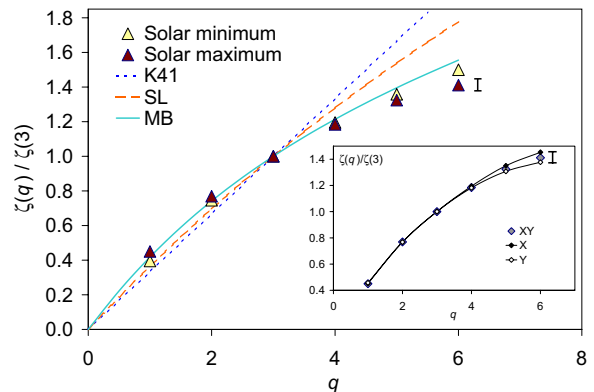


FIG. 4: ESS exponents as compared to the Kolmogorov  $q/3$  scaling (K41) and hierarchical models of IT defined in the text. Inset: solar maximum exponents obtained for horizontal (X), vertical (Y), and arbitrary (XY) orientations of the displacement vector  $\delta\mathbf{r}$ , as a test for isotropy. Error bars in both plots show the discrepancy between horizontal and vertical  $\zeta(6)$  estimates at solar max.

The functions  $S_q(l)$  exhibit ESS over almost the entire range (Fig. 3, inset). The relative ESS exponent  $\zeta(q)/\zeta(3)$  (Fig. 4) shows a clear departure from the Kolmogorov law. Both of these features are typical of IT systems. To highlight the origin of this intermittency, we have tested several analytical fits encompassed by a hierarchical model [41, 42]:

$$\zeta(q) = (q/g)(1-x) + C(1 - (1-x/C)^{q/g}) \quad (2)$$

The model contains three tuning parameters defined by

the relations  $\delta z \sim \ell^{1/g}$ ,  $t_e \sim \ell^x$ , and  $C = 3 - D$ , where  $t_e$  is the energy transfer time at smallest inertial scales  $\ell$  and  $D$  is the dimension of the dissipative structures. The She-Leveque (SL) model [43] with vortex filaments ( $D = 1$ ) is obtained substituting  $g = 3$ ,  $x = 2/3$ , and  $C = 2$ . The Iroshnikov-Kraichnan MHD model [44] assumes  $g = 4$ ,  $x = 1/2$ , and  $C = 1$  with dissipative structures interpreted as current sheets and predicts values of the relative exponents which for the  $q$  range considered here are indistinguishable from the SL model. The combination  $g = 3$ ,  $x = 2/3$ , and  $C = 1$  gives the Müller-Biskamp (MB) model [42] implying that turbulence occurs in a 3d MHD system with hydrodynamic scaling and sheet-like dissipative structures. As Fig. 4 shows, the latter provides the best overall description for our data.

Our main finding is the simultaneous appearance of robust signatures of both SOC and IT in a single time series of coronal images – including significantly different phases of the solar cycle. These observations can be interpreted using a variety of physical scenarios. One of them assumes that turbulence in coronal dissipation is passively driven by SOC avalanches of dissipating currents which modify the magnetic field and shape its intermittent spatial pattern [31]. A more collaborative interaction between SOC and MHD turbulence is also possible in which SOC avalanches of reconnecting magnetic loops [25, 30] generate inward and outward plasma flows [45] and/or cascades of MHD shock waves [46] working as sources of turbulence-driven anomalous resistivity regions which may affect the avalanches [13]

Among the key open problems is the one of the primary physical mechanism of the coronal avalanches. A plausible model has been proposed by Dahlburg et al. [14] who have shown that secondary instabilities needed to support the avalanche can be triggered by the misalignment between the reconnecting flux tubes. The model is based on sheet-like dissipative structures compatible with the MB turbulent cascade [42], and predicts rapidly evolving instabilities with the energy dissipation growth time of about 200 Alfvén transit times across the sheets [14]. These instabilities, reminiscent of toppling events in sandpiles [2], can propagate throughout extended coronal regions and lead to the multiscale explosive release of the coronal energy accompanied with SOC and IT signatures. Observational verification of this mechanism is a task for future research.

We thank V. Abramenko, A. Klimas and A. Pouquet for valuable discussions.

---

\* Electronic address: vuritsky@phas.ualgary.ca

[1] A. Kolmogorov, Dokl. Akad. Nauk SSSR **31**, 538 (1941).  
 [2] P. Bak et al., Phys. Rev. Lett. **59**, 381 (1987).  
 [3] G. Boffetta et al., Phys. Rev. Lett. **83**, 4662 (1999).  
 [4] V. Antoni et al., Phys. Rev. Lett. **87**, 045001 (2001).

[5] V. Carbone et al., Europhys. Lett. **58**, 349 (2002).  
 [6] P. Bak and M. Paczuski, Physica A **348**, 277 (2005).  
 [7] K. Chen and C. Jayaprakash, Physica A **340**, 566 (2004).  
 [8] K. R. Sreenivasan et al., Physica A **340**, 574 (2004).  
 [9] T. Chang, Phys. Plasmas **6**, 4137 (1999).  
 [10] M. Paczuski et al., Phys. Rev. Lett. **95**, 181102 (2005).  
 [11] P. Bak et al., Phys. Lett. A **147**, 297 (1990).  
 [12] M. Paczuski and P. Bak, Phys. Rev. E **48**, R3214 (1993).  
 [13] A. J. Klimas et al., J. Geophys. Res.–Space Physics **109**, 1426 (2004).  
 [14] R. B. Dahlburg et al., Astrophys. J. **622**, 1191 (2005).  
 [15] A. J. Klimas et al., e-print [astro-ph/0701486](https://arxiv.org/abs/astro-ph/0701486) (2006).  
 [16] P. Bak and C. Tang, J. Geophys. Res.–Solid Earth and Planets **94**, 15635 (1989).  
 [17] M. Paczuski et al., Phys. Rev. E **53**, 414 (1996).  
 [18] V. Frette et al., Nature **379**, 49 (1996).  
 [19] P. Dmitruk and D. O. Gomez, Astrophys. J. **484**, L83 (1997).  
 [20] F. Reale et al., Astrophys. J. **633**, 489 (2005).  
 [21] S. Galtier and A. Pouquet, Sol. Phys. **179**, 141 (1998).  
 [22] M. J. Aschwanden et al., Astrophys. J. **535**, 1027 (2000).  
 [23] D. Berghmans and F. Clette, Sol. Phys. **186**, 207 (1999).  
 [24] J.-P. Delaboudiniere et al., Sol. Phys. **162**, 291 (1995).  
 [25] P. Charbonneau et al., Sol. Phys. **203**, 321 (2001).  
 [26] M. J. Aschwanden and C. E. Parnell, Astrophys. J. **572**, 1048 (2002).  
 [27] C. E. Parnell and P. E. Jupp, Astrophys. J. **529**, 554 (2000).  
 [28] D. Berghmans et al., Astron. Astrophys. **336**, 1039 (1998).  
 [29] E. T. Lu and R. J. Hamilton, Astrophys. J. **380**, L89 (1991).  
 [30] D. Hughes et al., Phys. Rev. Lett. **90**, 131101 (2003).  
 [31] V. I. Abramenko and V. B. Yurchyshyn, Astrophys. J. **597**, 1135 (2003).  
 [32] V. M. Uritsky et al., J. Geophys. Res.–Space Physics **107**, 1426 (2002).  
 [33] V. M. Uritsky et al., Geophys. Res. Lett. **30**, 1813 (2003).  
 [34] E. N. Parker, Astrophys. J. **330**, 474 (1988).  
 [35] M. Baiesi et al., Phys. Rev. Lett. **96**, 051103 (2006).  
 [36] A. Corral and M. Paczuski, Phys. Rev. Lett. **83**, 572 (1999).  
 [37] C. Tang and P. Bak, J. Stat. Phys. **51**, 797 (1988).  
 [38] L. Biferale and I. Procaccia, Phys. Rep. **414**, 43 (2005).  
 [39] This choice is dictated by the logic of our study aimed at finding complementary SOC and IT signatures in a *single* emission field.  
 [40] R. Benzi et al., Phys. Rev. E **48**, R29 (1993).  
 [41] H. Politano and A. Pouquet, Phys. Rev. E **52**, 636 (1995).  
 [42] W.-C. Müller and D. Biskamp, Phys. Rev. Lett. **84**, 475 (2000).  
 [43] Z.-S. She and E. Leveque, Phys. Rev. Lett. **72**, 336 (1994).  
 [44] P. S. Iroshnikov, Sov. Astron. Zh. **40**, 742 (1963).  
 [45] N. Narukage and K. Shibata, Astrophys. J. **637**, 1122 (2006).  
 [46] M. Ryutova and T. Tarbell, Phys. Rev. Lett. **90**, 191101 (2003).  
 [47] The exponent  $D_A$  was estimated by counting the number  $N_A$  of non-overlapping boxes of size  $l$  needed to cover the activity at the peak of the avalanche, using  $N_A(l) \sim l^{-D_A}$ . The exponents  $z$  and  $D_A$  were obtained from regression plots  $T(A)$  and  $E(A)$  assuming  $A \sim l^{D_A}$ .  
 [48] This is usually done by plotting  $S_q(l)$  versus  $S_3(l)$